Assessment of ICESat-2's Horizontal Accuracy Using Precisely Surveyed Terrains in McMurdo Dry Valleys, Antarctica

Tony Schenk, Beata Csatho, *Member, IEEE*, and Tom Neumann

***Abstract*— This article presents an assessment of the horizontal accuracy and precision of the laser altimetry observations collected by NASA's Ice, Cloud, and Land Elevation Satellite-2 (ICESat-2) mission. We selected the terrain-matching method to determine the position of laser altimeter profiles within a precisely known surface, represented by a digital elevation model (DEM). We took this classical approach a step further, approximated the DEM by planar surfaces, and calculated the optimal position of the laser profile by minimizing the square sum of the elevation differences between reference DEMs and ICESat-2 profiles. We found the highly accurate DEMs of the McMurdo Dry Valleys (DV), Antarctica, ideal for this research because of their stable landscape and rugged topography. We computed the 3-D shift parameters of 379 different laser altimeter profiles along two reference ground tracks collected within the first two years of the mission. Analyzing these results revealed a total geolocation error (mean $+1\,\sigma$) of 4.93 m for version 3 and 4.66 m for version 4 data. These numbers are the averages of the six beams, expressed as mean $+1\,\sigma$ and lie well within the mission requirement of 6.5 m.**

***Index Terms*— Calibration, Ice, Cloud, and Land Elevation Satellite-2 (ICESat-2), laser altimetry.**

I. Introduction

NASA launched the Ice, Cloud, and Land Elevation Satellite-2 (ICESat-2), the successor of ICESat, on September 15, 2018 [1]. ICESat-2 carries the advanced topographic laser altimeter system (ATLAS) instrument, the first photon-counting lidar system for the purpose of elevation measurements from space [2]. ATLAS transmits six laser beams and records each photon's transit time to reconstruct surface height and structure along the satellite's ground track (GT). The ATLAS observations enable the estimation of ice-sheet mass balance and corresponding contributions to sea level rise [3]. Covering our entire planet, ICESat-2 also maps vegetation cover and structure, ocean elevations, and provides shallow coastal bathymetry and geodetic control for earth observations [4].

High accuracy of single-photon geolocation is needed to achieve the mission's primary goal of monitoring land-ice elevation (ice sheet and glaciers) and sea-ice freeboard changes on a centimeter-scale level. Considering the large extent of the Antarctic ice sheets, these stringent mission requirements are necessary because small changes in surface height have a considerable impact on mass balance and sea level change estimates. The mission requirement of 0.4 cm/yr for ice-sheet elevation change rates corresponds to 51 Gt/yr which is comparable to the uncertainty of current Antarctic ice-sheet mass balance estimates [5].

ICESat-2's horizontal geolocation error requirement of 6.5 m on the earth's surface translates to approximately 3 arc seconds directional error of the laser beam. The changes in sun-orbit geometry induce thermal–mechanical stress that causes time-varying misalignments between the components used to determine data geolocation, such as the motion between star trackers, the GPS antennas, and the ATLAS telescope [6]. This, in turn, requires sophisticated calibration procedures to keep the ever-changing errors under control. An excellent reference to the ICESat-2 calibration is provided by [6]. While the calibration identifies errors and corrects them, validation is only concerned with quantifying the errors. Post-launch assessments of ICESat-2 observations using corner-cube retro-reflectors and comparisons with precisely mapped terrains indicate a vertical precision of better than 10 cm and a horizontal accuracy within the mission requirement of 6.5 m [6]–[8].

Our primary concern in this article is the assessment of ICESat-2's single-photon horizontal geolocation accuracy and its temporal variation. We use the method of matching ICESat-2 elevations along GTs with precisely surveyed terrain. The horizontal accuracy is estimated by finding the geocoded signal photons' best agreement with the reference digital elevation model (DEM) through 3-D translations of the GTs. The knowledge of the horizontal accuracy is essential because it may introduce a secondary vertical error, as shown in equation $\sigma_v = \sigma_h \tan\alpha$ with σ_v the induced vertical error, σ_h the horizontal error, and α the slope angle. Suppose a horizontal error of ± 11 m (equals to the footprint size, [8]) and a typical slope angle at the ice-sheet margin of 1°, we obtain a secondary vertical error of

Manuscript received May 20, 2021; revised September 23, 2021 and December 28, 2021; accepted January 20, 2022. Date of publication January 31, 2022; date of current version March 17, 2022. This work was supported by the ICESat-2 Mission through the NASA Cryospheric Sciences Program under Award 80NSSC18K1289 and Award 80NSSC21K0915. *(Corresponding author: Tony Schenk.)*

Tony Schenk and Beata Csatho are with the Department of Geological Sciences, University at Buffalo, Buffalo, NY 14260 USA (e-mail: afschenk@buffalo.edu; bcsatho@buffalo.edu).

Tom Neumann is with the NASA Goddard Space Flight Center, Greenbelt, MD 20771 USA (e-mail: thomas.neumann@nasa.gov).

Digital Object Identifier 10.1109/TGRS.2022.3147722

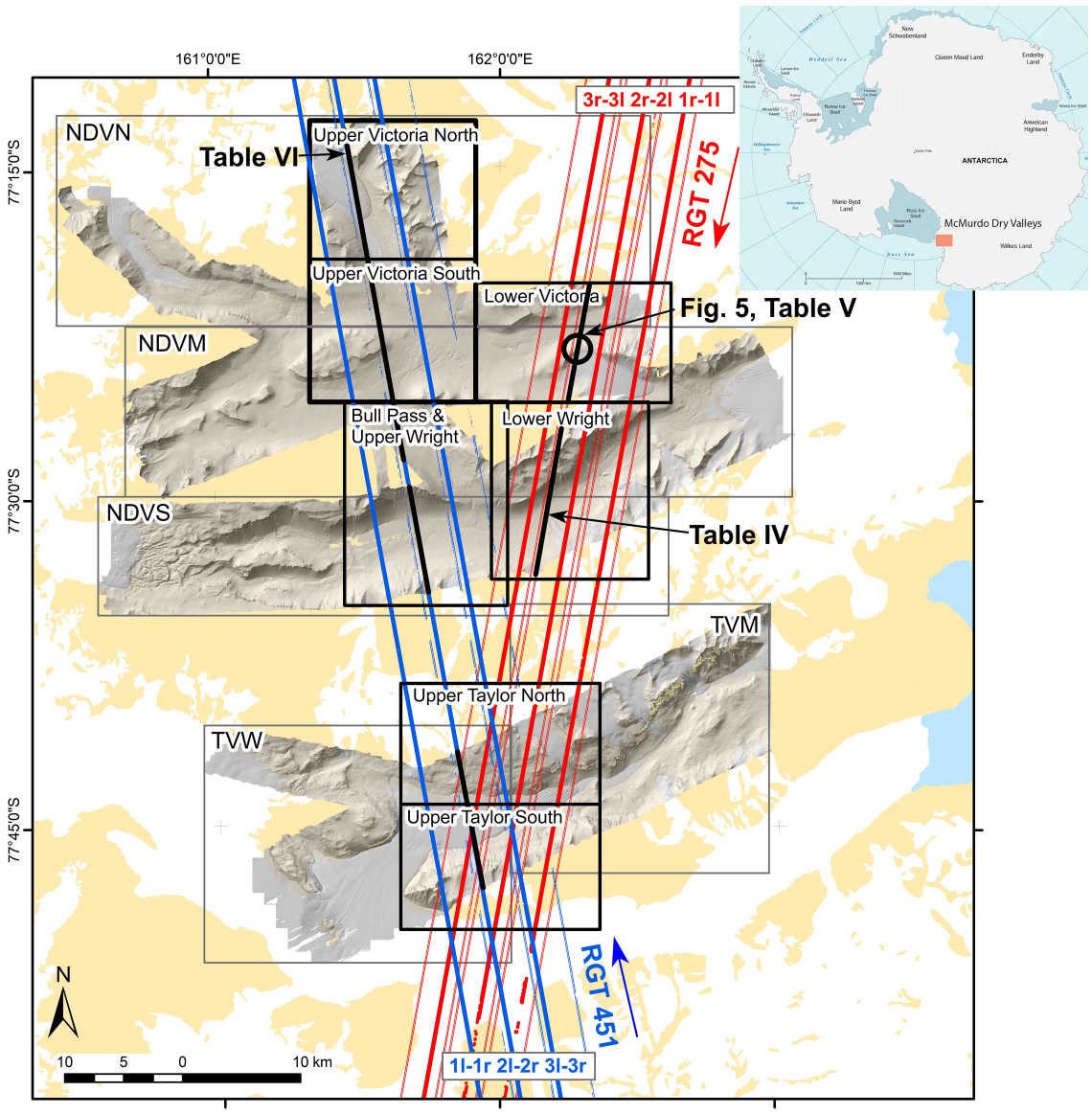

Fig. 1. Overview of the validation site in the MDV with inset in upper right showing MDV in Antarctica. NCALM DEMs used in this study are shown as shaded relief maps and delineated by thin black lines (Table I). DEMs covering RGTs 275 and 451 are generated from subsets of NCALM DEMs and their outlines are shown by thick black lines (Table II). Colored lines are ICESat-2 GTs used in this study: RGT 275 (cycles 1 and 2: thin, and 3 & 5–9 thick red lines) and 451 (cycles 1: thin and 3–9 thick blue lines). Yellow regions mark rock outcrops, white shows ice sheet and outlet glaciers, and blue is Ross Sea (from Antarctic Digital Database, 2000). GT sections highlighted by black are used in examples in Fig. 5, Tables IV–VI.

0.21 m—way above the anticipated vertical error of a few centimeters.

Section II introduces the McMurdo Dry Valleys (MDV) in East Antarctica that we used as our validation site, and Section III elucidates the mathematical concept of our approach. The later sections provide characteristic results, including a thorough error assessment. We also compare the results obtained with data from versions 3 and 4.

II. ICESat-2 Validation Site, McMurdo Dry Valleys, Antarctica

The terrain-matching method aims at finding a laser altimeter elevation profile in a known surface. The known reference surface, likely being represented by a DEM, must satisfy certain characteristics to apply this approach. For one, the horizontal accuracy of the DEM should be better than the altimeter system. Equally important is the requirement that no significant changes (e.g., erosion or vegetation growth) occur between the time the DEM is measured and the time it is used to calculate translation vectors of ICESat-2. The DEMs should also have a distinct topographic structure, for example, deep valleys, steep, and stable walls oriented in different directions. For frequent detection of time-varying biases of ICESat-2, the DEMs must be located in the polar regions where we have repeat passes of ICESat-2.

The DEMs that satisfy these stringent requirements are indeed available in the MDV, East Antarctica (Fig. 1, Table I). Low precipitation, no vegetation, and cold temperatures make the area a polar desert resulting in largely stable landscapes. The first survey of the MDV used NASA's Airborne Topographic Mapper (ATM) lidar system in the austral summer of 2000–2001 [9]. The DEMs calculated from the laser

TABLE I

DEMs OF MDV SELECTED FOR THIS STUDY FROM THE NCALM SURVEY IN 2014–15 [14]. ELEVATIONS ARE ON THE WGS-84 ELLIPSOID. ZONES ARE ACCORDING TO LANDSCAPE STABILITY, C: COASTAL THAW, M: INLAND MIXED, S" STABLE UPLAND [11], [13]

DEM Name	Abbr.	Geographic features	Elevation (m)	Zone
Northern DV North	NDVN	Victoria & Barwick Valleys	300–2070	C, M
Northern DV Middle	NDVM	McKelvey Valley, Wright Valley E., Bull Pass	125–1930	C, M, S
Northern DV South	NDVS	Wright Valley W, Labyrinth	-52–1925	C, M
Taylor Valley West	TVW	Taylor Valley, Taylor Glacier	270–1950	C, M
Taylor Valley Middle	TVM	Taylor Valley	10–1850	C, M

observations were successfully used for validating ICESat measurements [10].

However, increasing summer air temperatures in recent decades resulted in destabilization of buried ice and increased surface ablation of the valley glaciers [11], [12]. The most vulnerable regions are the coastal, ice-cored Ross Sea Drift deposits, and ice-cemented permafrost at the low-laying valley floors [11], [13]. Therefore, from December 2014 to January 2015, about 3600 km^2 was resurveyed by National Science Foundation's National Center for Airborne Laser Mapping (NCALM) to determine landscape changes as temperatures increased in the MDV [11]. As pointed out in [12] the comparison between ATM and NCALM DEMs revealed areas with substantial elevation differences (up to 1 m) due to thermokarst subsidence and glacier thinning, for example. Their research guided the selection of GTs for this study. We used NCALM DEMs for our ICESat-2 validation study as they were collected closer in time to the mission.

Along the coast, rapid erosion with rates reaching several meters per year was detected at several sites [12]. The processes causing these significant changes include deep incision of streams into buried ice and formation of thermokarst ponds and thaw slumps. Therefore, we excluded coastal region from this study (e.g., Taylor Valley E and Denton Hill DEMs, [14]).

The DEMs covering the selected reference GTs (RGTs 275 and 451) are located further inland, in the Inland Mixed Zone (Northern Dry Valleys (DV) North, Middle, and South; Taylor Valley Middle and West DEMs, Table I, Fig. 1). In this region, elevation changes were 0.05 m/yr or less, mainly caused by erosion and deposition along stream and river banks and outlet glacier mass balance changes. These changes, usually restricted to short segments of ICESat-2 GT, were neglected. However, increasing lake levels, attributed to increasing melt of glaciers and permafrost, were significant during the past few decades [12]. The largest change was detected on Lake Vanda (Wright Valley), where lake level increased with an average rate of 0.3 m/yr between 2000/01 and 2014/15. Therefore, we examined all solutions with segments over large lakes and discarded those with large uncertainties.

NCALM used Optech's Titan multispectral airborne laser scanner that rendered two to ten returns per m^2 [14]. The geographic coordinates (latitude, longitude) and the elevation of the laser points were calculated in the World Geodetic System, WGS84 ellipsoid, based on International Terrestrial Reference Frame (ITRF) 2008. The estimated vertical error of the individual laser points is $\pm$0.07 m root mean square error (RMSE) [14]. DEMs were derived at 1 m intervals on a regularly spaced grid in the US Geological Survey Transantarctic Mountains Projection (EPSG:3294) system. More detailed information about the laser campaign and data processing can be found in [14].

TABLE II

DEMs GENERATED FROM SUBSETS OF NCALM DEMs, TO COVER THE TWO RGTs, 275 AND 451, USED IN THIS STUDY (FIG. 1)

DEM Name	derived from
Upper Victoria Valley North	NDVN
Upper Victoria Valley South	NDVN & NDVM
Bull Pass & Upper Wright Valley	NDVM & NDVS
Lower Victoria Valley	NDVN & NDVM
Lower Wright Valley	NDVM & NDVS
Upper Taylor Valley North	TVM & TVW
Upper Taylor Valley South	TVM & TVW

To provide the best geometry and avoid extremely long segments, we combined parts of the original NCALM DEMs and subsetted them into new DEMs that better agree with landscape units, like valley floors with surrounding valley walls (Table II).

III. ICESAT-2 MISSION AND DATA DESCRIPTION

ICESat-2 orbits earth at 7 km/s at an average altitude of 500 km. The near-polar orbit has an inclination of 92°, producing a coverage between 88° north and south, with a 91-day exact repeat cycle in the polar regions [2]. The satellite carries ATLAS, a single-photon counting laser altimetry system [1], [2]. ATLAS uses a low-energy, green (532 nm) laser pulse that is split into six individual beams. Each beam illuminates a footprint on the earth's surface, diameter $\sim$11 m [8].

The six laser beams are arranged in three pairs: one central pair and two sideward looking pairs. Each pair consists of a strong and a weak energy beam with the latter approximately four times weaker. By slightly yawing the spacecraft, the array with the six beams is rotated with respect to the flight direction, causing the strong and weak beams of the pairs to be separated by $\sim$90 m (Fig. 2), thus enabling the determination of the across-track slope. The spot pairs are separated on the ground by $\sim$3.5 km across-track, and the strong and weak beams of each pair are $\sim$2.5 km from each other along-track [2]. Approximately every 8 months, the ICESat-2 observatory is reoriented by rotating it around its nadir axis to maximize sun illumination on the solar arrays. ICESat-2 was launched in forward orientation and then rotated to backward orientation on December 28, 2018 (yaw flip). Fig. 2 shows the numbering convention of the six beams in forward and backward orientations relative to the direction of travel.

An essential result of laser altimeter observations, such as performed by the ATLAS system of the ICESat-2 satellite,

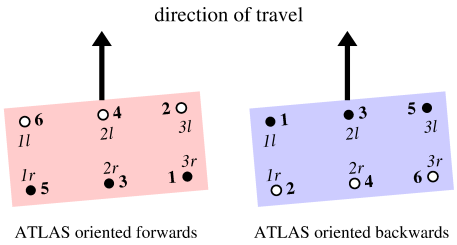

Fig. 2. Beam pattern and numbering convention of the six ATLAS beams, in forward and backward oriented settings. Numbers 1–6, in boldface, are related to the same physical beam, regardless of the array's orientation, while (1l, 1r), (2l, 2r), and (3l, 3r) refer to beam pairs 1 (left), 2 (center), and 3 (right) relative to the direction of travel of the satellite. Strong beams (1, 3, and 5) are marked with filled circles. Derived from [1], Fig. 8.

is to determine the location where the laser beam interacts with the earth's surface. This process is known as geolocating a laser beam and is accomplished with three fundamental measurements: 1) location of the origin of emitting a laser pulse,2) pointing direction of the beam, and3) the travel time of the pulse from its origin to the spot it illuminates on the ground and back to ATLAS again. The precision orbit determination (POD) of ATLAS aims at delivering the location of the spacecraft center of mass and the offset vectors to ATLAS [15]. Precision pointing determination (PPD) is tasked with the determination of the direction of the laser beam [16]. The horizontal accuracy of the location of the laser spot (or footprint) depends mostly on the uncertainty of the direction vector.

The ATLAS/ICESat-2 L2A Global Geolocated Photon Data (ATL03) product of the ICESat-2 mission contains the geolocation of each photon event downlinked from ATLAS [1], [2]. The geolocations are given as latitude, longitude, and elevation with respect to WGS84 ellipsoid based on ITRF2014. In addition, ancillary data are provided, such as landcover type (land ice, sea ice, land, ocean) and the classification of photon events into signal photons with different confidence levels and noise photons. According to this photon classification, Class 4 is assigned to high-confidence photons that were most likely reflected from the earth's surface. Classes 3 and 2 indicate signal photons with lower confidence levels. Class 1 is assigned to likely background photons to provide a buffer zone around the surface [1].

Since the DEMs are given in the United States Geological Survey (USGS) Transantarctic Mountains Projection (EPSG:3294) system, we adopted this system for all the computations. The difference between the ITRF systems used for the DEMs and ATL03, i.e., ITRF2008 versus ITRF2014, results in very small differences (mm level, personal communication, Andrew Fountain, 2020). Therefore, we did not apply a transformation to account for the different ITRFs. Also, because we are concerned in this study with the horizontal error of ICESat-2, small height differences do not impact our results.

From ATL03, higher level data products, such as the Land Ice Along-Track Height Product, ATL06 [17], yielding land-ice elevation at every 20 m along-track, are derived. Although its smaller data volume makes it easier to work with ATL06 data, we elected to use the ATL03 product. ATL03 includes pulses 0.7 m apart with a few signal photons in each pulse. Thus, it gives a more detailed representation of the terrain and increases the data redundancy in our algorithms, leading to more robust solutions. Section V-B provides a more detailed rationale for using the ATL03 data product.

TABLE III
TWO RGTS AND THE DATES WHEN CROSSING THE MDV. RGT 275 IS DESCENDING AND 451 IS ASCENDING. SEE FIG. 1 FOR LOCATION OF GTS

cycle	RGT 275	RGT 451
1	10/16/2018	10/28/2018
2	1/15/2019	1/22/2019
3	4/16/2019	4/27/2019
4		7/27/2019
5	10/14/2019	10/26/2019
6	1/13/2020	1/25/2020
7	4/13/2020	4/25/2020
8	7/13/2020	
9	10/12/2020	10/23/2020

ATL03 and ATL06 products, which are publicly available, were obtained from the National Snow and Ice Data Center (NSIDC) [18], [19]. We used observations collected from RGT 275 (descending) and 451 (ascending), cycles 1–9, covering a period of 10/16/2018 to 10/23/2020 (Table III). Most results in this study are derived from ATL03 data, version 4; however, we also used version 3 data to compare the horizontal accuracy of ICESat-2, obtained with data from both the versions.

Version 4 contained a number of data processing updates (alignment of the laser with respect to the spacecraft; alignment between the individual beams; improved spacecraft attitude solutions) that improved the overall geolocation uncertainty compared with version 3. Taken together, these improvements yield a translation of photon locations between releases when viewed at lengths scales less than a few hundred kilometers. At longer length scales, this translation varies gradually around the orbit and through the seasons.

IV. METHODOLOGY

The ATLAS system is a profiling system as opposed to a scanning system. This implies that the six laser beams are in fixed positions. Surface elevation profiles along GTs measured by the laser beams consist of a sequence of 3-D points, corresponding to geolocated photons, calculated from observed angles and positions of the platform, together with the range. We refer to these locations as laser points and call a segment of consecutive laser points a laser profile, represented as distance/height pairs. It is important to realize that the location of geolocated photons is not identical to the true (physical) location from where the photons are reflected back into space. The goal of this study is to provide a quantitative measure of the difference between true and estimated position. This is achieved by determining the location of best agreement of an ICESat-2 elevation profile within a precisely known DEM. The vector between this location and the geolocated photons is called **translation vector** in this study. Its magnitude is used to estimate the horizontal accuracy of the ATL03 data product.

The traditional approach of finding the location with the best agreement between a laser profile and a DEM is to

generate a DEM profile at the location of the laser profile (e.g., [8], [20], [21]). Then the height differences between the two profiles serve as a measure for the closeness. These steps are repeated at shifted locations until the point of best agreement is found. The problem with this traditional approach is that there is no direct way to predict where the location with the best agreement is and one is forced to compute the height differences at every point within the search space. More important is the fact that it is not obvious how one can derive rigorous error quantities of the location of best agreement.

A. Principle

We have modified the traditional approach by casting it as an ordinary least-squares adjustment. For obtaining an analytical function of the difference between laser and DEM profiles, we approximate the DEMs by planar surface patches in the vicinity of ICESat-2 GTs. The idea of approximating natural surfaces with analytical functions to find the best match of a laser profile in a DEM has been originally proposed by [22]–[24].

We summarize the ordinary least-squares method with a Gauss–Markov model as follows [25]:

$$\boldsymbol{A}\,\boldsymbol{x} = \boldsymbol{b} - \boldsymbol{r}, \tag{1}$$

$$\boldsymbol{W} = \boldsymbol{\Sigma}_b^{-1}, \tag{2}$$

$$\boldsymbol{N} = \boldsymbol{A}^T \boldsymbol{W} \boldsymbol{A}, \tag{3}$$

$$\boldsymbol{N}\hat{\boldsymbol{x}} = \boldsymbol{A}^T \boldsymbol{W} \boldsymbol{b}, \tag{4}$$

$$\hat{\boldsymbol{x}} = \boldsymbol{N}^{-1} \boldsymbol{A}^T \boldsymbol{W} \boldsymbol{b}, \tag{5}$$

$$\hat{\boldsymbol{b}} = \boldsymbol{A}\,\hat{\boldsymbol{x}}, \tag{6}$$

$$\hat{\boldsymbol{r}} = \boldsymbol{b} - \hat{\boldsymbol{b}}, \tag{7}$$

$$\sigma_o^2 = \frac{\hat{\boldsymbol{r}}^T \boldsymbol{W} \hat{\boldsymbol{r}}}{m - n}, \tag{8}$$

$$\boldsymbol{\Sigma}_{\hat{x}} = \sigma_o^2 \boldsymbol{N}^{-1}. \tag{9}$$

Equation 1 expresses the observation equations with $\boldsymbol{A}$ the observation equation matrix, $\boldsymbol{x}$ the vector with the unknowns, $\boldsymbol{b}$ the vector with the observations, and $\boldsymbol{r}$ the vector containing the residuals. Equation 2 is the weight matrix, $\boldsymbol{W}$, which is the inverse of the covariance matrix, $\boldsymbol{\Sigma}_b$, of the observations. If it is assumed that the observations are uncorrelated, then the covariances are zero, and $\boldsymbol{W}$ becomes a diagonal matrix with the inverse variances of the observations on the diagonal. Equation 3 is the normal equation matrix, and the following equation expresses normal equations. The next equations show the estimated solution of normal equations, $\hat{\boldsymbol{x}}$, the estimated observations, $\hat{\boldsymbol{b}}$, and the estimated residuals, $\hat{\boldsymbol{r}}$. Equation 8 expresses the estimated variance of unit weight with m the number of observations and n the number of unknowns. Finally, 9 is the covariance matrix for the unknowns, containing in the diagonal the estimated errors of the unknowns.

Now we specify the mathematical model for our problem to determine the location with the best agreement between a laser profile and a DEM. This involves the computation of planar surface patches of the DEM along the trajectory of an ICESat-2 GT. The three independent unknowns of a planar surface patch, e.g., two slope angles and one absolute height, can be found by fitting a plane through DEM grid points.

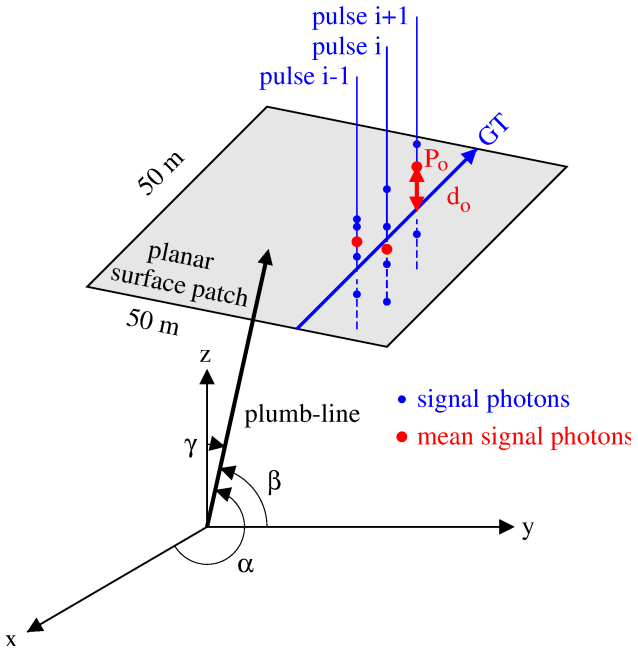

Fig. 3. Planar surface patch computed by fitting a plane through DEM grid points. Also shown is GT as the transect of laser pulses with the plane. The mean of signal photons is the average of all signal photons (categories 2–4). The mean is used as a representative value of the surface height.

In our study, we use the Hessian formula that directly gives the shortest distance from a point to a plane

$$d = x\cos\alpha + y\cos\beta + z\cos\gamma - \rho \tag{10}$$

where x, y, z are the the coordinates of the point, $\cos\alpha, \cos\beta, and \cos\gamma$ are the direction cosines shown in Fig. 3, ρ is the length of the plumb line (distance of the plane from the coordinate system's origin), and d is the distance from the point to the plane.

Fig. 3 sketches a planar surface patch and its representation in the Hessian formula. It also shows three laser pulses with signal photons and their respective means, a computed quantity used as a representative height of the surface.

To model the error of the laser system, we introduce in 10 an unknown translation vector $\boldsymbol{t} = (\Delta x,\ \Delta y,\ \Delta z)$ and obtain

$$d = (x + \Delta x)\cos\alpha + (y + \Delta y)\cos\beta + (z + \Delta z)\cos\gamma - \rho. \tag{11}$$

This equation is linear with respect to the unknown translation vector. Rearranging leads to the following linear observation equation of a least-squares adjustment:

$$\begin{aligned}\mathrm{res}_{ij} = {} & \Delta x\cos\alpha_j + \Delta y\cos\beta_j + \Delta z\cos\gamma_j \\ & + x_i\cos\alpha_j + y_i\cos\beta_j + z_i\cos\gamma_j - \rho_j\end{aligned} \tag{12}$$

where the index i runs from 1 to the total number of points in plane j and index j runs from 1 to the total number of planes involved. Since the adjustment problem is linear, no approximations of the three unknown components of the translation vector are necessary. Moreover, the adjustment delivers estimates not only for the unknowns but also for their errors.

B. Workflow

The workflow entails four major steps. In every step, the computations are repeated independently for all six beams of ICESat-2. The first processing step selects one GT and subsets it to the DEM. At the same time, it examines the ATL03 photon distribution for suitability for further processing. Large gaps in the data or obvious blunders may be reasons to reject GT. We pass on to the next processing step and use only signal photons of Class 2 or higher. Note that only one DEM/GT combination is used in the same processing step, referred to as a computational unit in this article. If the same GT traverses another DEM, a new translation vector will be computed.

The primary purpose of the second processing step is to analyze the signal photon distribution in each pulse. Under very favorable conditions, we may expect up to a dozen photons for strong beams and approximately one fourth of it for weak beams [2]. In case of multiple photons, we determine the average height and its standard deviation (σ) to estimate the surface height and its precision (see also Fig. 3). Multiple photon events also provide the opportunity to determine and eliminate blunders. The standard deviation serves as the weight for the surface height for pulse i, that is, the diagonal element of the weight matrix becomes $1/\sigma_i^2$.

In the third step, we are concerned with determining planes in the DEM along the trajectory of an ICESat-2 GT. The size of the bounded planes depends on the topography of the DEM, its sampling size, and the magnitude of the anticipated translation vector. Considering these factors, we have chosen a size of 50 m $\times$ 50 m for the surface patches. With a DEM grid spacing of 1 m, we have 2500 DEM grid points to fit a plane, thus guaranteeing robust estimates for the three unknown plane parameters and their errors. Planes with fitting errors greater than 1 m were rejected. In this step, we also solve the correspondence problem between ICESat-2 laser points and planar surfaces.

The fourth step consists of executing the least-squares algorithm described in Section IV-A. The result gives an estimate for the mean translation vector for the given computational unit and the error of this estimate. Since the adjustment is linear, no approximations for the unknown parameters are required and no iterations are necessary.

C. Additional Information

In order to facilitate the comparison of the translation vector with other results and to provide a direct relationship of the translation vector to ICESat-2's precision pointing system, we perform a fifth step to transform the horizontal coordinates to a local ground-track system (Fig. 4).

As the figure illustrates, the positive along-track axis points to the travel direction of the satellite and the positive across-track axis is perpendicular, pointing to the right of the travel direction. The across- and along-track axes form a right-handed coordinate system.

Table IV contains useful statistical information related to beams 3 (strong) and 4 (weak) of RGT 275, cycle 1, when it crosses the Lower Wright Valley DEM (Fig. 1). Remember from Section IV-B, the process of calculating the closest distance between an ICESat-2 profile and its corresponding DEM profile begins with selecting signal photons from the ATL03 dataset. There is usually more than one signal photon per pulse (Table IV, column 4). In that case, we take the mean as a representative value for the pulse. If only one signal photon per pulse is available, we compare it with signal photons of neighboring pulses and only accept it if the height difference is below a user selected threshold.

The DEM must be approximated by planar surface patches to enable a mathematical approach for determining the best fit of the ICESat-2 profile with the DEM (Section IV-A). Column 6 in Table IV contains the total number of accepted planar surfaces and the last column lists the total number of ATL03 laser points participating in the adjustment.

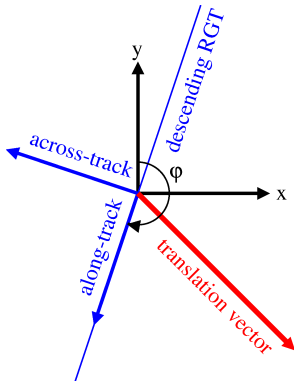

Fig. 4. Calculation of translation vector is performed in US EPSG:3294 x, y, z system and then transformed into the local across-track/along-track system.

TABLE IV
USEFUL INFORMATION ABOUT CENTRAL BEAM PAIR (BEAMS 3 AND 4) OF RGT 275, CYCLE 1, LOWER WRIGHT VALLEY DEM. GTS ARE HIGHLIGHTED IN FIG. 5 (BLACK LINE). COL. 2–4 SHOW THE TOTAL NUMBER OF SIGNAL PHOTONS, THE TOTAL NUMBER OF PULSES, AND THOSE WITH MORE THAN ONE SIGNAL PHOTON. THE LAST TWO COLUMNS LIST THE NUMBER OF PLANES AND OBSERVATIONS ASSOCIATED WITH PLANES

beam	total signal photons	total number pulses	pulses with signal photons > 1	total number planes	total number observations
3	64537	15623	12682	224	8979
4	19367	10405	5128	227	5991

V. RESULTS

A. Comparison of ICESat-2 Elevations and DEMs Before and After Adjustment

Fig. 5 illustrates the ICESat-2 measurements along a 900-m segment of RGT 275 as it crosses the Robinson Ridge between Victoria Valley and Clark Glacier on October 16, 2018 [Fig. 5(b)]. Selected is the strong beam of the central pair (beam 3 or GT2r, see Fig. 2, forward orientation). Fig. 5(a) shows the distribution of the geolocated photons (ATL03) and the land-ice elevation product (ATL06) over the crest of the ridge. The high confidence signal photons (Class 4) are shown by red dots, while low confidence signal photons in

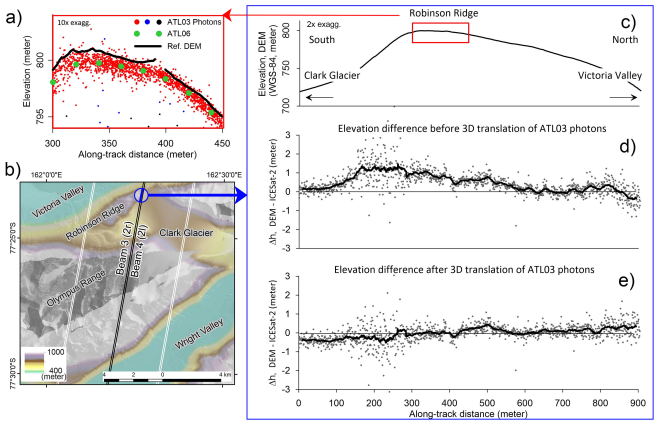

Fig. 5. Results from RGT 275, cycle 1, October 16, 2018, over the Robinson Ridge within the Lower Victoria Valley DEM (circled in Fig. 1). (a) Beam 3 (GT2l) classified signal photons across the Robinson Ridge (within red box in c): red dots: Class 4; blue dots: Class 3; black dots: Class 2 photons. Large green-filled circles are ATL06 elevations. Solid black line represents DEM elevation. (b) Location of ICESat-2 GTs shown on DEM (color), overlain on Sentinel-2 imagery (B/W), beams 3 and 4 are shown by black lines, and other GTs are white. Elevations from reference DEM and ICESat-2 beam 3 (GT2r) within blue circle are used in (c)–(e). (c) Topography from DEM along the GT of beam 3. (d) Elevation difference between the surface height estimated as the average of the signal photon heights for each pulse at the original geolocation of the ICESat-2 pulses and the reference DEM. Thick black line shows the difference smoothed by a moving average filter with a 20-m window. (e) Same difference as in (d) after the ICESat-2 photons are shifted according to the translation vector (see Section 3.2 for details).

Classes 3 and 2 are shown by blue and black, respectively. Large filled green circles refer to ATL06 data. The black line represents the surface elevation from the reference DEM at the original positions of the ATL03 photons along the GT.

As Fig. 5(a) shows, most of the ATL03 photons are below the DEM in this profile, underestimating the surface elevation compared with o the reference DEM by up to more than 1 m over the steepest slope [Fig. 5(d)]. Using our approach, we obtained a translation vector of $(3.15 \pm 0.07, -1.73 \pm 0.05, 0.24 \pm 0.01)$ m for the computational unit encompassing this ICESat-2 profile. After shifting the ATL03 photons with this translation vector, they show significantly improved agreement with the reference DEM, indicating that most of the horizontal error is removed [Fig. 5(e)]. The linear trend in the remaining difference could be attributed to short-term variations in ICESat-2 pointing errors. By assuming a constant translation vector within each DEM, our method only recovers the mean of this translation vector, but not its short-term variations.

B. Comparison of Translation Vectors Estimated From ATL03 and ATL06

We have also performed experiments with the ATL06 data product [17]. ATL06 is derived from ATL03 and is represented as an along-track data product at 20-m resolution. ATL06 also takes the additional step of correcting the asymmetry of the transmit pulse shape, together with correcting to remove the first-photon bias [17]. Despite these advantages, we have chosen ATL03 because its point density is much higher which leads to a more faithful representation of the surface.

TABLE V

DIFFERENCES IN TRANSLATION VECTORS COMPUTED WITH ATL03 AND ATL06 DATA, RGT 275, CYCLE 1, OCTOBER 16, 2018, ALL SIX BEAMS, LOWER VICTORIA VALLEY DEM [BLACK LINE IN FIG. 1)]. "ACROSS" AND "ALONG" REFER TO THE ACROSS-/ALONG-TRACK COORDINATE SYSTEM (FIG. 4)

beam	translation vector				difference	
	ATL03		ATL06		ATL03 - ATL06	
	across [m]	along [m]	across [m]	along [m]	across [m]	along [m]
1	1.186	-7.108	1.047	-7.287	0.139	0.179
2	-1.451	-1.993	-1.586	-2.108	0.135	0.115
3	-3.412	1.134	-3.514	1.043	0.102	0.091
4	-1.236	-2.211	-1.360	-2.337	0.124	0.126
5	-6.064	0.916	-6.325	0.862	0.261	0.054
6	0.431	-3.096	0.266	-3.118	0.165	0.022
mean	-1.758	-1.758	-1.912	-2.158	0.154	0.098
stdev	2.650	2.650	2.681	3.054	0.056	0.055

The 20-m interval of the ATL06 data may be an undersampling of more rugged surfaces. The confidence in the calculated translation vector increases with the number of surface patches used in the adjustment including the number of ICESat-2 laser points associated with a surface patch. We have to find a compromise between the number of DEM grid points used to approximate the surface patch (as many as possible), the fitting error of approximation (as low as possible), and the density of ICESat-2 GT (ATL03 or ATL06).

Suppose we select a surface patch size of 30 m × 30 m. This would render 900 DEM grid points to support the approximation by a plane. ATL06 would only have a maximum of two points associated with that surface patch. On the other hand ATL03 will have some 42 points covering the same patch, thus increasing the redundancy and making the adjustment much more robust.

The last two columns of Table V show the differences between the translation vector computed with the ATL03 and ATL06 data, respectively. These differences are rather small but not entirely random as the nonzero mean in the second last line and the positive sign of all six differences clearly show. A plausible reason for the bias is the fact that ATL06 is corrected for several geophysical and instrument errors while ATL03 is not. This might cause a vertical bias in our surface height estimated from ATL03, which, in turn, impacts the translation vector [7].

C. Representative Result, RGT 451, Cycle 3

Table VI lists the results of the central beam pair of RGT 451, cycle 3. This example is representative for the accepted translation vectors. DEM length refers to the length of the overlapping ICESat-2/DEM profile (computational unit) and the remaining two columns show the estimated errors of the translation vector. These errors are computed in the least-square solution of the translation vector and are based on the assumption that the observations (geolocations of ATL03 signal photons) are uncorrelated and their errors are normally distributed.

We determine the translation vector along an overlapping ICESat-2/DEM profile, the length of which depends on several

TABLE VI

ACROSS (AC) AND ALONG-TRACK (AL) COMPONENTS, AND THE LENGTH (MAG) OF THE TRANSLATION VECTORS AND THEIR ERRORS CALCULATED FOR THE CENTRAL BEAM PAIRS 3 AND 4, RGT 451, CYCLE 3, APRIL 27, 2019. DEMS INVOLVED: UVN = UPPER VICTORIA NORTH, UVS = UPPER VICTORIA SOUTH, BPUW = BULL PASS & UPPER WRIGHT, UTN = UPPER TAYLOR NORTH, UTS = UPPER TAYLOR SOUTH (FIG. 1)

beam	translation vector			DEM		accuracy		
	ac [m]	al [m]	mag [m]	name	length [km]	σ_{ac} [m]	σ_{al} [m]	σ_{mag} [m]
3	-1.71	1.43	2.23	UVN	11.1	0.07	0.06	0.09
	-1.86	0.72	1.99	UVS	12.4	0.02	0.10	0.10
	-2.02	1.27	2.39	BPW	16.3	0.01	0.14	0.14
	-3.61	0.99	3.75	UTN	4.1	0.02	0.13	0.13
	-1.42	0.82	1.64	UTS	7.2	0.02	0.09	0.09
4	-2.33	-1.13	2.59	UVN	11.1	0.11	0.09	0.14
	-1.94	-2.85	3.45	UVS	12.4	0.04	0.12	0.12
	-1.97	-2.60	3.26	BPW	16.3	0.01	0.27	0.27
	-2.13	-2.93	3.62	UTN	4.1	0.04	0.19	0.19
	-0.88	-3.16	3.28	UTS	7.2	0.04	0.09	0.10

factors such as a vivid topography with surface slopes oriented in distinctly different directions. The lengths of the profiles used in this study range between 4 and 16 km. Thus, it takes ICESat-2 1–2 s to traverse one DEM and less than 10 s to cross the entire region of the MDV.

We assume that within such short time intervals, only small, high-frequency (jitter) variations have an impact on the geolocation of ICESat-2. These vibrations are at a higher rate than can be captured by the PPD algorithm (i.e., frequency > 20 Hz) and are due to the coupling between mechanical systems on the spacecraft (beam-steering mechanism, reaction wheels, solar array dive assembly) and the structure of the observatory. More information about spacecraft line-of-sight jitter management and mitigation can be found in [26].

The schematic of Fig. 6 depicts a 5-s-long interval along an ICESat-2 GT, crossing three DEMs. The red line symbolizes high-frequency noise that impacts the translation vectors (blue solid circles), determined in the least-squares adjustment (Table VI). We can conceive these values as the means of the translation vectors that are influenced by the high-frequency variations within short time spans as ICESat-2 crosses individual DEMs.

D. Entire Dataset, RGTs 275 and 451

We processed a total of 405 translation vectors and accepted 379 that satisfied the following criteria: kappa < 20, $\sigma_{across} < 1$ m, $\sigma_{along} < 1$ m. Kappa (ratio of maximum eigenvalue over minimum value) is a good indicator for the stability of the normal equation system.

Fig. 7 depicts the temporal relationship of the translation vectors of all the beams for RGTs 275 and 451, during 739 days of the mission (nine cycles). Several dots plotted at the same time indicate that a GT traversed several DEMs during the same repeat cycle. The differences between the translation vectors are attributed to short-term variations discussed in Section V-C. For example, beam 3 of RGT 451, cycle 3, crossed five DEMs, resulting in five translation vectors (see also Table VI).

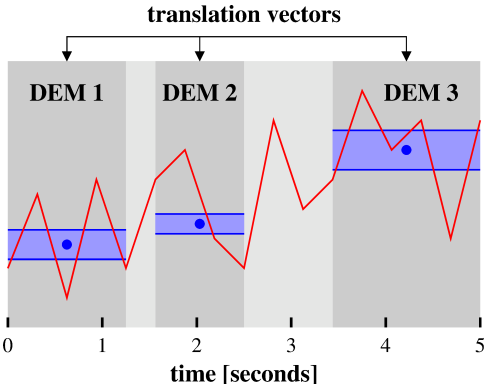

Fig. 6. A 5-s-long (35 km) GT crossing three DEMs. The red line symbolizes the horizontal error of ATL03, including a high-frequency noise (jitter) component. Blue solid circles indicate the computed translation vectors. Dark blue bands centered at translation vectors symbolize uncertainties of the translation vectors.

VI. ASSESSMENT OF ICESAT-2 GEOLOCATION ERRORS

As pointed out in Section I, we are concerned with assessing the horizontal accuracy and precision of ICESat-2 observations. This is important because a horizontal error will induce a secondary vertical error, proportional to the horizontal error multiplied by the slope of the terrain.

Since the horizontal error of the reference DEM is <0.3 m [14], the length of the translation vector that minimizes the difference between the surface topography calculated from the ATL03 geolocated signal photons and the reference DEMs can be used as an estimate of ICESat-2's horizontal accuracy. To achieve the ICESat-2 mission requirement, this error should be below 6.5 m. Our goal is to check whether the latest version of ATL03 products satisfies this condition.

We now turn our attention to long-term variation in the ICESat-2 horizontal error, estimated from 379 translation vectors, considering the entire observation interval of 739 days. The results are summarized in Fig. 7 and Table VII. Statistics (mean and standard deviation for each beam and all beams), characterizing the ICESat-2 geolocated photons' horizontal errors, for versions 3 and 4, are shown in columns 2–7. The total error refers to mean $+1\ \sigma$. Also added to the table are results reported by [6], obtained with version 3 data.

Comparing the results of versions 3 and 4 from this study shows only a modest improvement of ICESat-2 horizontal accuracy (total errors in columns 4 and 7, 4.93 m versus 4.66 m). However, there is a significant drop in the standard deviation of the horizontal error for all the beams (σ) from 1.09 to 0.62 m, suggesting that the horizontal errors of the six ICESat-2 beams determined from version 4 data are more narrowly distributed than from version 3 data. Both the versions show beam 1 having the largest error and beam 5 the smallest error. The horizontal error of beams 1, 2, and 4 decreased significantly from version 3 to 4 (10%–20%), while errors of beams 2, 5, and 6 remained unchanged or slightly increased, The visual inspection of Fig. 7 reveals that no trend can be discerned over the entire observation period of 739 days.

When comparing the version 3 data reported in Table VII with those reported by [6], also obtained with version 3, one

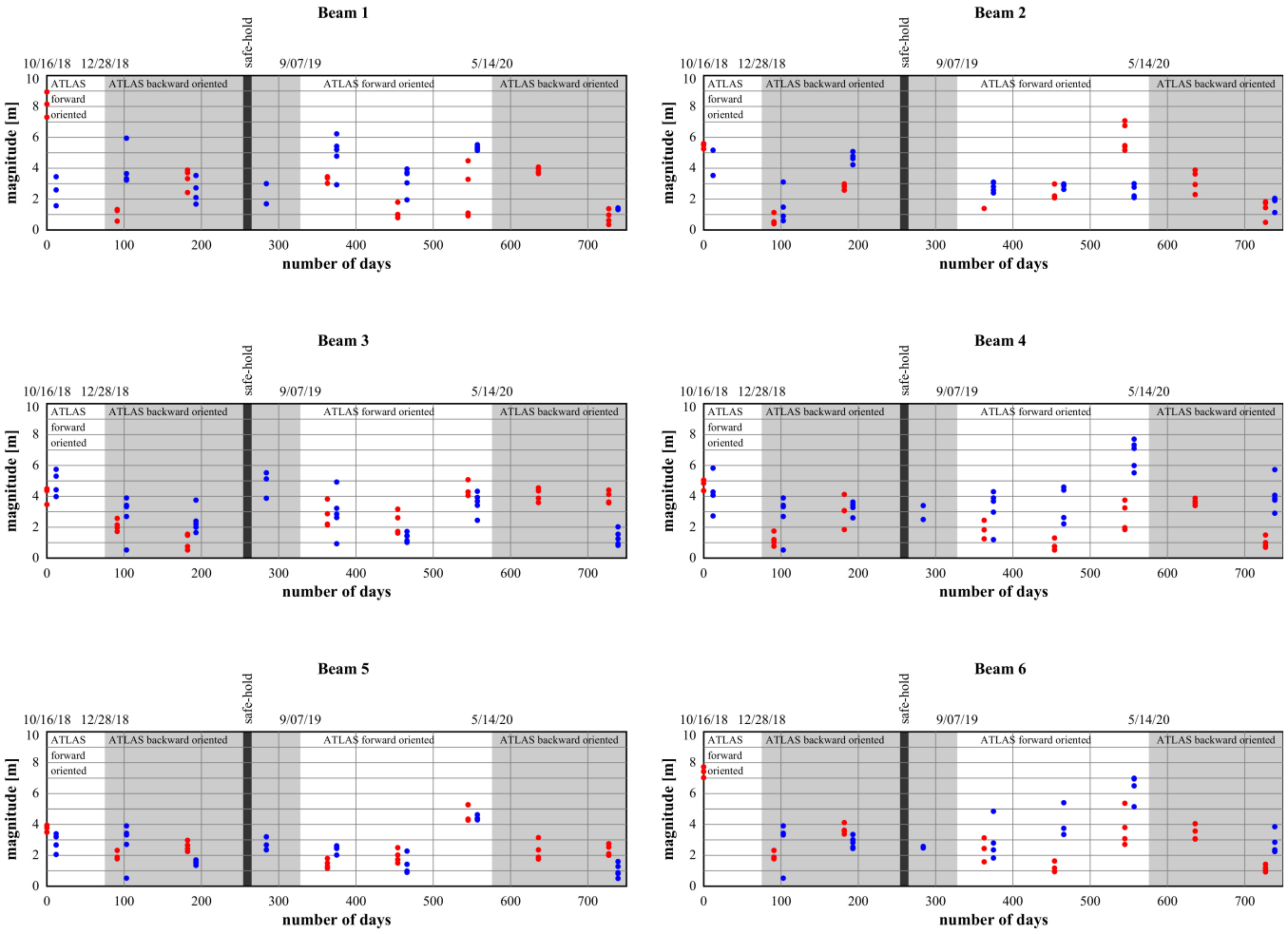

Fig. 7. Magnitude (length) of translation vector as a function of time, estimating ICESat-2 horizontal geolocation errors for all six beams. Red dots are results from RGT 275 (descending) and blue dots refer to ascending RGT 475. Time is shown as MMDDYY (top of panel) and in number of days (bottom). The observation interval spans October 16, 2018, to October 23, 2020, cycle 1 through 9, for a total of 739 days. Accuracy of the magnitude of translation vector is on the order of 0.05–0.25 m (Table VI) and too small to show.

TABLE VII

GEOLOCATION ERRORS OF ICESAT-2. RESULTS ARE ARRANGED IN THREE GROUPS: VERSION 3 AND 4 (THIS STUDY) AND FROM ARCTICDEM [6]. NUMBERS REFER TO THE LENGTH OF THE TRANSLATION VECTOR (MAGNITUDE)

beam number	version 3			version 4			reported by [6]		
	mean [m]	σ [m]	total error [m]	mean [m]	σ [m]	total error [m]	mean [m]	σ [m]	total error [m]
1	4.12	2.26	6.38	3.28	2.05	5.33	2.4	1.8	4.2
2	3.82	1.88	5.70	2.97	1.63	4.60	3.2	1.6	4.8
3	2.77	1.11	3.88	2.97	1.38	4.34	1.7	1.1	3.8
4	3.54	1.80	5.34	3.20	1.69	4.89	1.8	1.5	3.3
5	2.45	1.10	3.56	2.48	1.14	3.62	1.7	1.1	2.8
6	3.16	1.61	4.78	3.35	1.83	5.17	1.5	1.0	2.5
mean	3.31	1.63	4.93	3.04	1.63	4.66	2.05	1.35	3.40
σ	0.64	0.46	1.09	0.32	0.32	0.62	0.64	0.33	0.91

should bear in mind some important differences in how the two datasets are computed, e.g., the geographic region and its extent (entire ArcticDEM versus MDV Antarctica), the different methods used to determine ICESat-2 track offsets, and the horizontal accuracy of DEMs. Looking at the estimated ICESat-2 horizontal errors, one can conclude that they are, perhaps surprisingly, rather small and well within the 6.5-m geolocation requirement. We also note that the values from [6] are consistently lower than those from this study. This could be attributed to the fact that including ICESat-2 observations over the entire Arctic generates a multitude of data and thus lowers the error.

Although the results presented so far look very promising, we should not forget that they are obtained over a relatively

small region of earth. In order to figure out how local or global our results are, future research should include suitable test sites at different locations on earth.

VII. Discussion and Concluding Remarks

The prime objective of this article is to assess the horizontal accuracy of ICESat-2. We have improved the traditional method of matching a laser profile with a precisely known surface, likely being represented as a DEM, by casting it as a least-squares adjustment. This novel approach does not only offer the calculation of the 3-D translation vector but also provide rigorous information about error quantities related to the unknowns.

We have selected the MDV, East Antarctica, as our known surface because the DEMs are very accurate (1-m resolution, 0.07-m RMSE), have very stable landscape, and distinct topographic features. We have chosen two ICESat-2 RGTs from versions 3 and 4, cycles 1–9. Every GT crosses up to five DEMs. The least-squares adjustment was calculated independently for the six beams leading to a total of 379 accepted solutions of the 3-D translation vectors. The translation vector is a very suitable measure to assess the horizontal accuracy of ICESat-2. Our major results include: 1) the average horizontal error of the ICESat-2 beams estimated from all the translation vectors using the latest version 4 is about 4.66 m, well within NASA's specification of 6.5 m; 2) the relatively large variation in the translation vectors within an observation interval of less than 10 s—the time it takes ICESat-2 to traverse the Dry Valleys—indicates a significant horizontal error due to high-frequency jitter; 3) we also note that the temporal behavior is quite different for the individual beams, even within the same beam pair.

Our ICESat-2 horizontal accuracy estimates (average of 4.66 m with individual beam errors ranging from 3.62 to 5.33 m, version 4) show a remarkable agreement with those presented by [8] and [6]. We extended the study of [8] both spatially and temporarily. The MDV are 2000 km from their Antarctic site (Array 4, 88°S traverse, East Antarctica). We have a total of 16 distinct dates (two RGTs, each with eight accepted cycles) compared with the three dates examined by [8]. For the first time, we investigated the temporal variation in ICESat-2's horizontal error on-orbit during a two-year period with different sun-orbit geometry. Our results indicate a horizontal error of 4.66 m one sigma (Table VII, version 4 data), similar to prelaunch estimates [1].

To shed some light on the question of how valid the results of this study are, on a global scale, we propose that future work shall concentrate on repeating this research in other parts of the world. Additionally, we would like to extend the observation period to find analytical functions for modeling the temporal variation in the translation vectors. We have treated the translation vectors independently for the six beams, neglecting any constraints that may be applicable from a deeper knowledge on how the beams are physically arranged.

Appendix

The appendix contains the ICESat-2 granules used in this study.

TABLE VIII
RGT 275 and RGT 451 Granules

RGT	C	Date	Granule
275	1	Oct 16 2018	ATL03_20181016155531_02750110_001_01
275	2	Jan 15 2019	ATL03_20190115113516_02750210_001_01
275	3	Apr 16 2019	ATL03_20190416071512_02750310_001_01
275	5	Oct 14 2019	ATL03_20191014223446_02750510_003_01
275	6	Jan 13 2020	ATL03_20200113181430_02750610_003_01
275	7	Apr 13 2020	ATL03_20200413135418_02750710_003_01
275	8	Jul 13 2020	ATL03_20200713093405_02750810_003_01
275	9	Oct 12 2020	ATL03_20201012051351_02750910_003_01
451	1	Oct 28 2018	ATL03_20181028044356_04510112_003_01
451	2	Jan 27 2019	ATL03_20190127002352_04510212_003_01
451	3	Apr 27 2019	ATL03_20190427200335_04510312_001_01
451	4	July 27 2019	ATL03_20190727154312_04510412_003_01
451	5	Oct 26 2019	ATL03_20191026112310_04510512_003_01
451	6	Jan 25 2020	ATL03_20200125070255_04510612_003_01
451	7	Apr 25 2020	ATL03_20200425024243_04510712_003_01
451	9	Oct 23 2020	ATL03_20201023180215_04510912_003_01

Acknowledgment

The authors thank Prashant Shekhar and Ivan Parmuzin for preprocessing the ICESat-2 ATL03 and ATL06 data. The authors would also like to thank Andrew Fountain for helpful discussions about NCALM DEMs that were obtained from the Polar Geospatial Center, University of Minnesota.

References

[1] T. A. Neumann *et al.*, "The ice, cloud, and land elevation satellite–2 mission: A global geolocated photon product derived from the advanced topographic laser altimeter system," *Remote Sens. Environ.*, vol. 233, Nov. 2019, Art. no. 111325.

[2] T. Markus *et al.*, "The ice, cloud, and land elevation satellite-2 (ICESat-2): Science requirements, concept, and implementation," *Remote Sens. Environ.*, vol. 190, pp. 260–273, Mar. 2017.

[3] B. Smith *et al.*, "Pervasive ice sheet mass loss reflects competing ocean and atmosphere processes," *Science*, vol. 368, no. 6496, pp. 1239–1242, Jun. 2020.

[4] L. Magruder *et al.*, "New Earth orbiter provides a sharper look at a changing planet," *Eos*, vol. 100, Sep. 2019. [Online]. Available: https://eos.org/science-updates/new-earth-orbiter-provides-a-sharper-look-at-a-changing-planet

[5] A. Shepherd *et al.*, "Mass balance of the Antarctic ice sheet from 1992 to 2017," *Nature*, vol. 558, no. 7709, pp. 219–222, Jun. 2018.

[6] S. B. Luthcke *et al.*, "ICESat-2 pointing calibration and geolocation performance," *Earth Space Sci.*, vol. 8, no. 3, Mar. 2021, Art. no. e2020EA001494.

[7] K. M. Brunt, T. Neumann, and B. E. Smith, "Assessment of ICESat-2 ice sheet surface heights, based on comparisons over the interior of the antarctic ice sheet," *Geophys. Res. Lett.*, vol. 13, no. 2, pp. 7–615, 2019.

[8] L. A. Magruder, K. M. Brunt, and M. Alonzo, "Early ICESat-2 on-orbit geolocation validation using ground-based corner cube retro-reflectors," *Remote Sens.*, vol. 12, no. 21, pp. 21–3653, Nov. 2020.

[9] B. Csatho *et al.*, "Airborne laser scanning for high-resolution mapping of Antarctica," *Eos, Trans. Amer. Geophys. Union*, vol. 86, no. 25, p. 237, 2005.

[10] C. F. Martin, R. H. Thomas, W. B. Krabill, and S. S. Manizade, "ICESat range and mounting bias estimation over precisely-surveyed terrain," *Geophys. Res. Lett.*, vol. 32, no. 21, pp. 1–4, 2005.

[11] A. G. Fountain, J. S. Levy, M. N. Gooseff, and D. Van Horn, "The McMurdo dry valleys: A landscape on the threshold of change," *Geomorphology*, vol. 225, pp. 25–35, Nov. 2014.

[12] J. S. Levy *et al.*, "Decadal topographic change in the McMurdo dry valleys of Antarctica: Thermokarst subsidence, glacier thinning, and transfer of water storage from the cryosphere to the hydrosphere," *Geomorphology*, vol. 323, pp. 80–97, Dec. 2018.

[13] J. S. Levy *et al.*, "Accelerated thermokarst formation in the McMurdo dry valleys, Antarctica," *Sci. Rep.*, vol. 3, no. 1, pp. 1–8, Dec. 2013.

[14] A. G. Fountain *et al.*, "High-resolution elevation mapping of the McMurdo dry valleys, antarctica, and surrounding regions," *Earth Syst. Sci. Data*, vol. 9, no. 2, pp. 435–443, Jul. 2017.

[15] S. B. Luthcke, T. Pennington, B. D. Loomis, T. Rebold, and T. C. Thomas, "Ice, cloud, and land elevation satellite 2 (ICESat-2) project algorithm theoretical basis document for precise orbit determination, orbit design, and geolocation parameter calibration, version 2," NASA, Goddard Space Flight Center, Greenbelt, MD, USA, Tech. Rep., 2019. [Online]. Available: https://icesat-2.gsfc.nasa.gov/science/data-products

[16] S. Bae, L. Magruder, N. Smith, and B. Schutz, "Ice, cloud, and land elevation satellite 2 (ICESat-2) project algorithm theoretical basis document for precision pointing determination (POD), version 2," NASA, Goddard Space Flight Center, Greenbelt, MD, USA, 2019. [Online]. Available: https://icesat-2.gsfc.nasa.gov/science/data-products

[17] B. Smith *et al.*, "Land ice height-retrieval algorithm for NASA's ICESat-2 photon-counting laser altimeter," *Remote Sens. Environ.*, vol. 233, Nov. 2019, Art. no. 111352.

[18] T. Neumann *et al.*, "ATLAS/ICESat- 2 L2A global geolocated photon data, version 4," NASA Nat. Snow Ice Data Center Distrib. Active Archive Center, Boulder, CO, USA, Tech. Rep., 2019. [Online]. Available: https://nsidc.org/data/ATL03

[19] B. Smith *et al.*, "ATLAS/ICESat-2 L3A land ice height, version 3," NASA Nat. Snow Ice Data Center Distrib. Active Archive Center, Boulder, CO, USA, 2019. [Online]. Available: https://nsidc.org/data/atl06

[20] M. A. Hofton, J. B. Blair, S. B. Luthcke, and D. L. Rabine, "Assessing the performance of 20–25 m footprint waveform LiDAR data collected in ICESat data corridors in Greenland," *Geophys. Res. Lett.*, vol. 35, no. 24, Dec. 2008, Art. no. L24501.

[21] X. Tang, J. Xie, X. Gao, F. Mo, W. Feng, and R. Liu, "The in-orbit calibration method based on terrain matching with pyramid-search for the spaceborne laser altimeter," *IEEE J. Sel. Topics Appl. Earth Observ. Remote Sens.*, vol. 12, no. 3, pp. 1053–1062, Mar. 2019.

[22] S. Filin and B. Csathó, "Improvement of elevation accuracy for mass-balance monitoring using in-flight laser calibration," *Ann. Glaciol.*, vol. 34, pp. 330–334, 2002.

[23] S. Filin, "Recovery of systematic biases in laser altimetry data using natural surfaces," *Photogramm. Eng. Remote Sens.*, vol. 69, no. 11, pp. 1235–1242, Nov. 2003.

[24] S. Filin, "Calibration of spaceborne laser altimeters—An algorithm and the site selection problem," *IEEE Trans. Geosci. Remote Sens.*, vol. 44, no. 6, pp. 1484–1492, Jun. 2006.

[25] G. Strang and K. Borre, *Linear Algebra, Geodesy, and GPS*. Wellesley, MA, USA: Wellesley-Cambridge Press, 1997.

[26] C. J. Dennehy, A. A. Wolf, and D. K. Swanson, "Spacecraft line-of-sight jitter management and mitigation lessons learned and engineering best practices," NASA STI Program Report Series, NASA Langley Res. Center, Hampton, VA, USA, Tech. Rep. NASA/TM-20210017871, 2021.

Tony Schenk received the M.S. degree in geodesy, photogrammetry, and cartography and the Ph.D. degree from the Swiss Federal Institute of Technology (ETH), Zürich, Switzerland, in 1965 and 1972, respectively.

From 1972 to 1974, he was a Research Scientist with ETHZ before he became the Division Head and the Senior Scientist with Leica, Heerbrugg, Switzerland. In 1985, he accepted the position of Professor of photogrammetry with The Ohio State University, Columbus, OH, USA, where he worked until his retirement in 2010. He holds a Research Professor appointment with the Department of Geology, University at Buffalo, Buffalo, NY, USA, and The State University of New York, Buffalo, NY, USA. He is an author, a coauthor, and an editor of several books and has over 180 publications. His research interests are in digital photogrammetry, computer vision, and geospatial information science with an emphasis on object recognition and surface reconstruction.

Dr. Schenk is a member of the American Society of Photogrammetry and Remote Sensing and the American Geophysical Union. He has held numerous offices, including in the International Society of Photogrammetry and Remote Sensing (ISPRS), where he was the President of a Technical Commission from 1996 to 2000.

Beata Csatho (Member, IEEE) received the M.S. degree in mathematics from Eötvös Loránd University, Budapest, Hungary, in 1989, and the M.S. and Ph.D. degrees in geophysics from the University of Miskolc, Miskolc, Hungary, in 1981 and 1993, respectively.

From 1981 to 1994, she was a Research Scientist with the Eötvös Loránd Geophysical Institute, Budapest, and the Byrd Polar Research Center, The Ohio State University, Columbus, OH, USA, from 1994 to 2006. In 2006, she joined the faculty of the Department of Geology, University at Buffalo, Buffalo, NY, USA, and The State University of New York, Buffalo, where she is a Chair and a Professor. She served as a Science Team Member of NASA's ICESat and IceBridge Missions and she is a Science Team Member of the ICESat-2 Mission. Her research interest includes glaciology, remote sensing, geophysics, spatial statistics, and data fusion.

Dr. Csatho is a member of the American Geophysical Union., IEEE, and the International Glaciological Society. She is a Scientific Editor of the *Journal of Glaciology*. She was the recipient of a Fulbright Fellowship in 1992, the Presidentś Honorary Citation and a Certificate of Appreciation from the International Society of Photogrammetry and Remote Sensing (ISPRS) in 2000 and 2001, and the NASA's Group Achievement Awards in 2004 and 2011.

Tom Neumann received the B.A. degree from the University of Chicago, Chicago, IL, USA, in 1996, and the Ph.D. degree from the University of Washington, Seattle, WA, USA, in 2003.

Since 2008, he has been with the NASA Goddard Space Flight Center, Greenbelt MD, USA, where he leads the ICESat-2 Mission as the Project Scientist. His background is in ice-sheet science, and he has published on various aspects of ice-sheet growth, decay, and motion. He has lead or participated in 11 science expeditions in Greenland and Antarctica.